creative commons
COMMONS DEED

저작자표시-비영리-변경금지 2.0 대한민국

이용자는 아래의 조건을 따르는 경우에 한하여 자유롭게

- 이 저작물을 복제, 배포, 전송, 전시, 공연 및 방송할 수 있습니다.

다음과 같은 조건을 따라야 합니다:

저작자표시. 귀하는 원저작자를 표시하여야 합니다.

비영리. 귀하는 이 저작물을 영리 목적으로 이용할 수 없습니다.

변경금지. 귀하는 이 저작물을 개작, 변형 또는 가공할 수 없습니다.

- 귀하는, 이 저작물의 재이용이나 배포의 경우, 이 저작물에 적용된 이용허락조건을 명확하게 나타내어야 합니다.
- 저작권자로부터 별도의 허가를 받으면 이러한 조건들은 적용되지 않습니다.

저작권법에 따른 이용자의 권리는 위의 내용에 의하여 영향을 받지 않습니다.

이것은 이용허락규약(Legal Code)을 이해하기 쉽게 요약한 것입니다.

Disclaimer

dCollection

이학석사 학위논문

QBO Influence on MJO Convection in a Numerical Weather Prediction Model

수치 모델에서 나타난 QBO 의 MJO 조절효과

2020 년 2 월

서울대학교 대학원

지구환경과학부

백 승 윤

Abstract

A series of observational studies have shown that the Madden-Julian Oscillation (MJO) in boreal winter is significantly modulated by the Quasi-Biennial Oscillation (QBO). The MJO becomes anomalously strong during the easterly QBO (EQBO) winters but weaken during the westerly QBO (WQBO) winters. In this study, the causal relationship is tested by integrating the Weather Research and Forecasting (WRF) model with varying lateral boundary conditions. The MJO event on December 2007, which was in the EQBO winter, is chosen as a reference case. The control ensemble-mean experiment (EQBO run) qualitatively reproduces the observed MJO. When the lateral boundary conditions are switched with those for the WQBO winter (WQBO run), the MJO event becomes weaker than the EQBO run with a pronounced weakening over the Maritime Continent. All eight ensemble members exhibit a smaller amount of precipitation over the Maritime Continent in the WQBO run than in the EQBO run. This result hints at a causal relationship in which the MJO strength is likely modulated by the QBO. The possible mechanism is briefly discussed.

Keywords : Madden-Julian Oscillation, Quasi-Biennial Oscillation, WRF
Student Number : 2018-24809

Table of Contents

List of tables ..... **i**

List of figures ..... **ii**

1. Introduction **1**

2. Data, Methodology, and Model Configuration **5**

2.1 Observational datasets **5**

2.2 Model details and configuration **5**

2.3 Experimental designs **7**

3. Results **9**

3.1 Comparison between the model simulation and observational data **9**

3.2 QBO forcing in the model and its representation **12**

3.3 The MJO convection difference between the EQBO and WQBO experiments **14**

3.4 The vertical structure difference between the EQBO and WQBO experiments **16**

4. Conclusions and Discussion **20**

5. References **24**

6. Tables **28**

7. Figures **30**

Abstract in Korean **44**

List of tables

Table 1. The Weather Research and Forecasting (WRF) model configuration for the 2007 December MJO event. The physics scheme, dynamics scheme, and boundary conditions are identical to those of Wang et al. (2015).

Table 2. Ensemble members and their initialization times, which are used in this study.

List of figures

Figure 1. (a) Time-height diagram of zonal wind (shading: m s^{-1}) averaged over 50–150°E, 5°S–5°N from January 2007 to December 2008 and (b) MJO phase diagram with OMI index from November 24 to December 31, 2007.

Figure 2. Time-longitude diagrams of (a) precipitation (shading: mm day^{-1}, contour: 15 mm day^{-1}), (b) outgoing longwave radiation (OLR) (shading: W m^{-2}), (c) 850-hPa and (d) 200-hPa zonal wind (shading: m s^{-1}) averaged over latitudes of 15°S–5°N based on observational datasets.

Figure 3. Time-longitude diagrams of (a) precipitation (shading: mm day^{-1}, contour: 15 mm day^{-1}), (b) OLR (shading: W m^{-2}), (c) 850-hPa and (d) 200-hPa zonal wind (shading: m s^{-1}) averaged over latitudes of 15°S–5°N based on the EQBO experiments.

Figure 4. The time-series of precipitation (left column: mm day^{-1}) and OLR (right column: W m^{-2}) in the Indian Ocean (upper panel), west of the Maritime Continents (middle panel), and the Maritime Continents (lower panel).

Figure 5. The longitude-height diagrams of pressure velocity (shading: Pa s^{-1}) and zonal distribution of precipitation (blue line: mm day^{-1}) and OLR (red line: W m^{-2}) averaged over latitudes of 15°S–5°N. Each composite map is averaged for four days from December 1 to 31, 2007. The left and right columns show the observations and EQBO experiments, respectively.

Figure 6. The vertical profile of zonal wind (unit: m s^{-1}) and temperature (unit: K) averaged over latitudes of 5°S–5°N in the western (50°E) and eastern (150°E) boundary of the model from November 24 to December 31, 2007.

Figure 7. The time-height diagrams of zonal wind (leftmost column: m s^{-1}) and temperature (second rightmost column: K) averaged over latitudes of 5°S-5°N in the EQBO (upper panel) and WQBO (middle panel) experiments and the difference between the two experiments from November 25 to December 29, 2007. The vertical profile of (f) zonal wind in the EQBO and WQBO experiments and (h) the temperature difference between the EQBO and WQBO experiments averaged from November 24 to December 31, 2007.

Figure 8. Time-longitude diagrams of (a)-(c) precipitation (shading: mm day^{-1}, contour: 15 mm day^{-1}), (d)-(f) OLR (shading: W m^{-2}), (g)-(i) 850-hPa and (j)-(l) 200-hPa zonal wind (shading: m s^{-1}) averaged over latitudes of 15°S–5°N from the EQBO and WQBO experiments and the difference between the two experiments.

Figure 9. The longitude-latitude diagrams of precipitation (shading: mm day^{-1}). Each composite map is averaged from for four days beginning on December 1, 2007. The left, middle and right columns show the EQBO, WQBO, and the difference between the two experiments, respectively.

Figure 10. The longitude-height diagrams for the 15°S–0° averaged relative humidity (shading: %) and zonal distribution of precipitation (blue line: mm day^{-1}) and OLR (red line: W m^{-2}). Each composite map is averaged for four days beginning on December 1, 2007. The left middle and right columns show the EQBO, WQBO, and the difference between the two experiments, respectively.

Figure 11. The longitude-height diagrams for the 15°S–5°N averaged temperature deviation from the domain zonal mean (shading: K) and zonal distribution of OLR (black line: W m^{-2}). Each composite map is averaged for four days beginning on 1 December 2007. The left panel and figure show the composite map in the EQBO and WQBO experiments, respectively.

1. Introduction

The Madden-Julian Oscillation (MJO; Madden and Julian, 1971, 1972; Zhang, 2005) is the typical intra-seasonal variability in the tropical troposphere. The MJO consists of enhanced and suppressed convection, and it propagates eastward from the Indian Ocean to the Western Pacific. The MJO not only impacts the tropics but also the mid-latitudes through its teleconnection (Zhang, 2013). This intra-seasonal variability can reduce the gap between the climate and synoptic scale by its timescale (Waliser et al., 2006). Therefore, the understanding of MJO is instrumental in improving seasonal-to-subseasonal (S2S) predictability (Zhang, 2013; Board et al., 2016).

Recent studies have revealed that the MJO can be modulated by the quasi-biennial oscillation (QBO), which is the interannual variability in the tropical stratosphere (Nishimoto and Yoden, 2017; Son et al., 2017; Yoo and Son, 2016). The QBO index and outgoing longwave radiation (OLR)-based MJO index (OMI) have a negative correlation in boreal winter. In other words, the MJO convection during the easterly phase of the QBO (EQBO) winter is stronger than that during the westerly QBO (WQBO) winter. Moreover, the MJO persists longer and propagates slower during the EQBO winter than during the WQBO winter (Son et al.,

2017; Zhang and Zhang, 2018). This relationship also appears in the operational and S2S models. The MJO prediction skill is higher during EQBO than WQBO in both the operational and S2S models (Marshall et al., 2017; Lim et al., 2019). This relationship between the QBO and MJO can improve the S2S predictability, and therefore, understanding the mechanisms of the QBO-MJO connection is very important.

One study suggests that the QBO can modulate the intensity of tropical tropospheric convection (Collimore et al., 2003). If the stratosphere has an EQBO (WQBO) phase, the upper troposphere and lower stratosphere (UTLS) have negative (positive) wind shear. From this wind shear, upward (downward) motion is found in the tropics by maintaining a thermal wind balance. The upward (downward) motion can change the tropical tropopause, which can lead to changes in tropical convection.

The role of the static stability in the UTLS for understating the mechanism of the QBO-MJO connection was highlighted in recent studies. Since the static stability in the UTLS region is lower during EQBO winter than during WQBO winter, the MJO convection is stronger during EQBO winter than during WQBO winter (Yoo and Son, 2016). Furthermore, during EQBO winter, the cirrus clouds in the UTLS region are more abundant than during WQBO winter. These cirrus clouds make

the upper troposphere warmer, which leads to weaker static stability in the UTLS region (Son et al., 2017). In addition, the cold cap in the UTLS during the EQBO winter is stronger and broader than that during the WQBO winter. The difference in thermal structures can lead to a difference in static stability and MJO convection (Hendon and Abhik, 2018).

There are some hypotheses on the mechanism of the QBO-MJO connection, but these hypotheses need to be verified. An efficient way to clarify the mechanism is by using the numerical weather prediction model. Many studies have tried to simulate the MJO by using the climate model to perform a model study (Lin et al., 2006; Hung et al., 2013; Ahn et al., 2017). However, even if the model simulates MJO well, there is a possibility that the model may not simulate QBO, and few models show the QBO-MJO connection (Lee and Klingaman, 2018; Butchart et al., 2018).

For these reasons, the model studies of the QBO-MJO connection use the cloud-resolving model. Martin et al. (2019) performed EQBO and WQBO simulations by imposing QBO-related zonal wind and temperature anomalies. From this model study, the QBO-related temperature has a more crucial role than the QBO-related zonal wind in the QBO-MJO connection. However, this cloud-resolving model only

considers the single column convection and thus has some difficulties in analyzing the detailed MJO structure.

The studies analyzing the detailed MJO structure mainly use the Weather Research and Forecasting (WRF) model. Wang et al. (2015) simulated two MJO events in October and November 2011 using the WRF model. After Wang et al. (2015), many model studies were performed to understand the initiation and propagation of MJO (i.e., Zhang et al., 2017; Chen et al., 2019). The WRF model has sufficient variables for analyzing the spatial and vertical structures of the MJO.

In this study, we try to reveal the QBO-MJO convection in a regional WRF model. We provide different QBO initial and lateral boundary conditions to evaluate the QBO-MJO relationship. From these model results, we examine a small hint of the physical and dynamical mechanisms on the QBO-MJO mechanisms. The observational datasets and model configuration are described in Section 2. The model performance in simulating MJO, the model boundary forcing and model response to QBO, as well as the QBO-MJO relationship in the model are described in Section 3. The conclusions and discussion are laid out in Section 4.

2. Data, Methodology, and Model Configuration

2.1 Observational datasets

The 6-hourly ERA-Interim data (Dee et al., 2011) are used to provide the initial and boundary conditions of the model for the MJO simulation and to verify the model's performance. It has a 0.75° x 0.75° horizontal resolution and 37 vertical layers. In addition, the TRMM 3B42 version 7A precipitation data with a horizontal resolution of 0.25° x 0.25° are used to evaluate the precipitation in the model. Clouds and the Earth's Radiant Energy System (CERES; Wielicki et al., 1996; Loeb et al., 2012) 1° synoptic (SYN1deg) data are used to evaluate OLR in the model. All of the data used are from November 24 to December 31, 2007.

2.2 Model details and configuration

In this study, the Weather Research and Forecasting model version 3.4.1 (WRF3.4.1; Skamarock et al., 2008) is used for the MJO simulation. The physics and dynamics scheme of the model are described in Wang et al. (2015), and the settings used in the model are shown in Table 1. The model has a 9 km horizontal resolution and consists of 45 vertical layers with a model top of 20 hPa. The boundary condition acts with a

narrow transition zone of 5 grid points by prescribing the tendencies, which are merged with the tendencies generated by the model. Spectral nudging (zonal wavenumber 0-4, meridional wavenumber 0-2) is applied to the horizontal wind for the first three days. The surface boundary conditions and sea surface temperature are prescribed every 6 hours. Please refer to Wang et al. (2015) for more information about the model configuration.

There are two large differences from the study by Wang et al. (2015): *1. Research period, 2. Computational domain*. First, Wang et al. (2015) simulated two MJO events in October and November 2011, which are not sufficient to analyze the QBO-MJO connection because these events did not occur in boreal winter. Therefore, we attempt to simulate an MJO case during boreal winter, when the QBO-MJO connection appears. Figure 1a shows the time-height diagram of daily zonal wind averaged over the equatorial region (50–150°E, 5°S–5°N) in the observational data. The easterly began to develop at 10 hPa in January 2007 and propagated to the lower stratosphere. In December 2007, strong easterly appeared in the lower stratosphere, showing EQBO conditions in the stratosphere. In addition, the MJO phase diagram with the OMI index represents an MJO event from November 24 to December 31 (Figure 1b). The QBO and MJO indices during this

period are the fifth strongest in comparison with other years (not shown).

Second, we expand the computational domain to be wider than Wang et al. (2015). The QBO-MJO connection is observed for all MJO phases, but the difference between the EQBO and WQBO is greatest when the MJO phase is 4, which is where the enhanced convection is located on the Maritime Continents (MC) (Yoo and Son, 2016). However, Wang et al. (2015) only covered the equatorial Indian Ocean (40–120°E, 20°S–20°N). There are some difficulties when examining the MJO intensity difference in the MC. Therefore, in this study, the computational domain was set to 50–150°E, 20°S–20°N, which covers from the Indian Ocean to the MC.

Accordingly, this experiment is carried out by expanding the computational domain to the MC area in the winter of 2007, which is when there was an MJO event with the EQBO background. All experiments consist of eight ensemble members whose initialization time differs from 00 UTC on November 20 at 12-hour intervals. Table 2 shows the initialization time for each ensemble. The integration time of the model is from the initialization time of each ensemble to 18 UTC on 31 December. All results in the text represent the ensemble-averaged results, and all ensemble members show similar results.

2.3 Experimental designs

We set up the WQBO experiment to reveal the QBO modulation on the MJO convection. The WQBO experiment is carried out almost identically to the EQBO experiment that simulated the MJO in December 2007, but with different boundary and initial conditions. The Lanczos filtering is applied to extract the QBO signals (1.5–3 years) from the state variables (horizontal wind field, temperature, geopotential height, and relative humidity) that act as initial and lateral boundary conditions. Considering the calculation time, we use interpolated 1.5° x 1.5° daily ERA-Interim data from 6-hourly 0.75° x 0.75° ERA-Interim data in subtracting the QBO signals. To consider the effects of the UTLS, the QBO signal above 300 hPa was extracted. The extracted QBO signals have an EQBO condition, and the QBO subtracted data have a WQBO condition. The experiment that uses these data as the initial and boundary conditions are named WQBO experiments.

3. Results

3.1 Comparison between the model simulation and observational data

The longitude-time diagrams of precipitation, OLR, 850-hPa, and 200-hPa zonal wind averaged over 15°S–5°N in the observational dataset are shown in Figure 2. The longitude-time diagrams of precipitation and OLR show that the MJO initiates over the Indian Ocean (50°E) on December 4 and propagates eastward with a speed of 6 m s^{-1} until December 28 (Figures 2a-b). The locations of precipitation and convection correspond to the convergence of 850-hPa zonal wind and the divergence of 200-hPa zonal wind (Figures 2c-d). This finding is consistent with the conceptual model of MJO suggested by Madden and Julian (1972).

The longitude-time diagrams of precipitation, OLR, 850-hPa, and 200-hPa zonal wind averaged over 15°S–5°N in the EQBO simulation are shown in Figure 3. The precipitation in the EQBO simulation is weaker than the observational precipitation in the Indian Ocean. On the other hand, the precipitation in the EQBO simulation is slightly stronger than the observational precipitation in the MC. Despite the model bias of precipitation, precipitation in the EQBO simulation shows eastward

propagation with similar MJO phase speeds. Likewise, OLR in the EQBO simulation also shows a similar model bias and eastward propagation. However, the EQBO simulation overestimates the OLR and has lower variability than the observations.

To check the precipitation and OLR response in different regions, time series of the precipitation and OLR in the Indian Ocean (15°S–5°N, 60–85°E), west of MC (15°S–5°N ,75–100°E), and MC (15°S–5°N, 130–150°E) are shown in Figure 4. The precipitation and OLR of the observational dataset in the Indian Ocean are 25 mm day^{-1} and 160 W m^{-2} near December 10, respectively. On the other hand, the EQBO simulation does not simulate this precipitation and convection. Despite the underperforming MJO in the Indian Ocean, the EQBO simulation perform the MJO well in the MC. The precipitation of observational data and the EQBO simulation in the MC are 20 mm day^{-1} and 25 mm day^{-1}, respectively. In addition, the OLR of the EQBO simulation is overestimated and shows lower variability than the observations. However, the tendencies of OLR are similar to the tendencies of the observations.

The appearance of regional differences in precipitation and convection in the Indian Ocean and MC of the EQBO simulation is due to the lower-level and upper-level wind fields (Figures 3c-d). As with the

observations, the EQBO simulation shows that the precipitation coincides with the convergence (divergence) of lower (upper) zonal wind. However, the EQBO simulation shows weaker lower (upper) zonal wind convergence (divergence) in the Indian Ocean and stronger lower (upper) zonal wind convergence (divergence) in the MC than in the observations. This zonal wind difference may cause the convection intensity difference by the convergence and divergence of tropospheric wind.

The 4-day mean longitude-height diagrams of pressure velocity and zonal distribution over the latitudes of 15°S–5°N from December 1 to December 28 are shown in Figure 5. The pressure velocity in the Indian Ocean shows upward motion from December 1 to December 8. This upward motion propagates eastward, and the precipitation and convection move eastward with the upward motion. However, the upward motion in the EQBO simulation is not found during the same period, and precipitation and the convection do not appear. The upward motion, related to the MJO in the EQBO simulation appears on December 13, and the upward motion, precipitation, and convection in the EQBO simulation are similar to the observations during the same time. However, the upward motion in the EQBO simulation is stronger than the observation near the MC. The center of the upward motion in

the EQBO simulation is higher than the observation from December 25 to 28.

From these results, the EQBO simulation does not simulate the MJO in the Indian Ocean, but it simulates the MJO more strongly than the observations on the MC. The horizontal wind convergence and divergence in the lower and upper troposphere are weaker in the Indian Ocean. However, the location and propagation speed of the MJO in the EQBO simulation are similar to the observations, and the tendency of the precipitation and OLR in the EQBO simulation is similar to the observations on the MC. In short, the EQBO simulation qualitatively simulates the MJO. In addition, we assume that the bias of the EQBO simulation occurs in all other simulations, and we modify the QBO background to check the MJO response.

3.2 QBO forcing in the model and its representation

The vertical structure of the zonal wind and temperature averaged over 5°S–5°N in the western (50°E) and eastern (150°E) boundary is shown in Figure 6. This is averaged from November 24 to December 31, and the blue, red, and black lines represent the forcings of the EQBO simulation, WQBO simulation, and the difference between the two simulations (doubled QBO signal), respectively. The maximum zonal

wind is shown at 30 hPa in the western and eastern boundaries in the EQBO simulation forcing. The stratospheric zonal wind in the WQBO, which is subtracted from the EQBO boundary forcing, is shown as a westerly. The maximum difference between the two simulations also appears at 30 hPa, showing -25 m s^{-1}, and -30 m s^{-1} at the western and eastern boundaries, respectively.

The temperature forcing difference between the two simulations is shown in 50 hPa, which is lower than 30 hPa, where the maximum zonal wind forcing difference appears. The maximum difference between the two simulations is approximately -3 K at 50 hPa at the western and eastern boundaries. The lower stratospheric zonal winds in the EQBO and WQBO simulations are easterly and westerly, respectively. The temperature of the UTLS in the EQBO simulation is colder than that in the WQBO simulation. The result is similar to the vertical structure of the zonal wind and temperature, according to the QBO in Son et al. (2017).

The vertical profiles of zonal wind and temperature from the EQBO and WQBO simulations are shown in Figure 7 to evaluate whether the model has represented the QBO well. The zonal wind averaged over 5°S–5°N, 50–150°E from November 24 and December 31, 2007 is found to the easterly and the westerly in the lower stratosphere for the whole

period. The largest zonal wind difference is approximately -25 m s^{-1} at 50 hPa. This means that the model simulates the QBO phase well.

In addition, in the vertical profile of the temperature in the two simulations, the temperature difference appears in the UTLS region. Similar to the model forcing, the temperature of the UTLS region in the EQBO simulation is colder than the WQBO simulation in the whole period. The largest difference in temperature is found at -2.5 K at 70 hPa. The largest difference in zonal wind and temperature in the model representation appears at lower altitudes than the model forcing. The difference between the model forcing and model response may be due to the sponge layer in the model top, which is located at 20 hPa. However, the vertical profiles of the two simulations are similar to those in Figure 6, which is represented in the model forcing. Therefore, we confirm that the EQBO and WQBO simulations represent the QBO phase well, and we check the QBO-MJO connection in the WRF model.

3.3 The MJO convection difference between the EQBO and WQBO experiments

The longitude-time diagrams of precipitation and OLR averaged over 15°S–5°N in the EQBO and WQBO simulations are shown in Figure 8. Both simulations captured the MJO initiation in the Indian Ocean and

eastward propagation. In this case, the MJO initiation time, location, and propagation speed show no difference between the two simulations. However, the intensity of convection between the two simulations is different, except in the Indian Ocean. Instead, the Indian Ocean precipitation in the WQBO simulation is greater than that of the EQBO simulation, which is different from previous studies. In contrast, the precipitation response near MC in the EQBO simulation is stronger than that in the WQBO simulation. This difference appears to be approximately 10% higher than the actual precipitation of up to 4.5 mm day^{-1} on December 20. The difference between the two simulations not only appears in the precipitation but also in the OLR. Similar to the precipitation, the OLR in the Indian Ocean does not show much difference but shows a rather strong convection in the WQBO, and the MJO convection near the MC is stronger in the EQBO simulation than in the WQBO simulation (Figures 8d-f).

The longitude-time diagrams of the 850-hPa and 200-hPa zonal wind averaged over 15°S–5°N are shown in Figures 8g-l, to evaluate the convergence and divergence of the lower and upper troposphere. The 850-hPa westerlies in the EQBO simulation are stronger than those in the WQBO simulation. However, the 850-hPa easterly in the EQBO simulation is weaker than that in the WQBO simulation. Consequently, it

is difficult to conclude that the 850-hPa convergence is activated in the EQBO simulation. Nevertheless, the 200-hPa zonal wind in the EQBO simulation shows a stronger structure than the WQBO simulation. The divergence in the upper troposphere in the EQBO simulation is stronger than that in the WQBO simulation, which leads to stronger activation of the MJO.

The spatial distribution of the 4-day averaged precipitation from December 1 to December 28 is shown in Figure 9, to examine the region where the MJO precipitation difference reaches the maximum. Both simulations show that the MJO initiates in the Indian Ocean, and detours to the south of the MC from December 13 to 16. This is one of the characteristics of the MJO that appears in the observations during the boreal winter (Kim et al., 2017). The precipitation difference is not found in the Indian Ocean, and the precipitation response in the EQBO simulation is stronger than that in the WQBO simulation from December 21 to 28. The largest difference appears in the west of New Guinea and north of Australia. This feature is also found in the OLR (not shown).

3.4 The vertical structure difference between the EQBO and WQBO experiments

We found that the MJO convection near the MC in the EQBO simulation is stronger than that in the WQBO simulation. Therefore, what dynamical structure led to the difference between the two simulations in terms of MJO activity in the MC? First, the vertical cross-section of the 4-day mean relative humidity averaged over 15°S–5°N from December 1 to 28 is shown in Figure 10 to examine the moisture difference between the two simulations, which has an important role in MJO initiation and propagation. The relative humidity structures are similar in both simulations. In both experiments, the relative humidity over 50% is found to reach up to approximately 100 hPa where the MJO convection is presented, and the propagation of this highly formed convection is clearly found. However, the relative humidity difference between the two simulations appears from December 9 to 12. The MJO-related relative humidity in the EQBO simulation is larger than the relative humidity in the WQBO simulation during this period. The relative humidity difference between the two simulations is approximately 8% when centered at 300 hPa. This relative humidity difference becomes larger after December 12. The relative humidity difference between the two simulations turns into approximately 10% at 300-500 hPa from December 13 to 20. In short, the relative humidity difference in the upper troposphere between the EQBO and WQBO

simulations occurs beginning at approximately 100°E, and the region where the maximum humidity difference appears gradually moves to 140°E around December 24. Similar to the relative humidity, the differences between the precipitation and OLR between the two simulations are found to move along the region where the maximum value of the relative humidity difference between the two simulations appears. Thus, the EQBO simulation has a wetter upper troposphere than the WQBO simulation, and this may create the difference in MJO intensities between the two simulations.

Consistent with the relative humidity difference in the upper troposphere between the two simulations, the temperature anomaly, which is the deviation from the zonal mean temperature (in this model experiment, the deviation from the zonally averaged temperature), also shows a difference between the two simulations in UTLS. The 4-day mean longitude-height cross-section of the temperature anomaly averaged over 15°S–5°N is shown in Figure 11. Both experiments show a similar structure, and the warm and cold anomalies near 100 hPa make a pair beginning on December 10. The cold anomalies near 100 hPa may play a role in intensifying the MJO convection by destabilizing the static stability near the upper troposphere. The temperature anomalies at 70 hPa precede the OLR by approximately 10 days (not

shown), which indicates that the temperature anomalies in the UTLS lead to MJO convection. The intensities of cold anomalies near 100 hPa and the warm anomalies located below the cold anomalies in the EQBO simulation are larger than those in the WQBO simulation beginning on December 9. In short, the WRF model captures the temperature anomaly differences between the two simulations well, which may induce the MJO convection difference.

4. Conclusions and Discussion

This study simulates an MJO case in December 2007 using the WRF model. The MJO properties, such as the propagation speed and location of the MJO, are well captured in the control (EQBO) simulation, despite some model bias related to the MJO intensity. In the same model setting as the EQBO simulation, the WQBO experiment is conducted by varying only the initial and boundary conditions from the background of the WQBO. Comparing the two simulations, the EQBO simulation indicates a stronger MJO intensity in the MC region for all variables, such as precipitation, OLR, and 850-hPa and 200-hPa zonal winds, than the WQBO simulation. The stronger upper zonal wind divergence in the EQBO simulation than in the WQBO simulation leads to stronger MJO precipitation and convection. The convection in the EQBO simulation is more active in the upper troposphere than in the WQBO simulation. This may be caused by the vertical thermal structure in the UTLS region, where the static stability in the EQBO simulation is lower than that in the WQBO experiment. Therefore, the model shows the QBO-MJO connection well in the model, but this study cannot easily test the significance of the differences between the two experiments due to the small sample size. Some points also need to be discussed, such as

significance testing.

In this study, the MJO intensity difference according to QBO in the MC region is well represented as in the previous study. However, the QBO-MJO relationship was not found in the Indian Ocean region, unlike previous studies. This may be because the MJO has not been well simulated in the Indian Ocean. The vertical thermal structure of the MJO from December 1 to 8 (Figure 11), in which the structure appears quite weak, may not induce MJO convection. The poor MJO performance in the Indian Ocean is thought to increase the uncertainty in terms of discussing the results between the two experiments.

In addition, there is a limitation that the QBO-MJO relationship between the two experiments is weaker than the actual observation. There are two main reasons for this limitation. First, this limitation may be due to the characteristics of the model, where the response of the model is smaller than in the real world. Second, this limitation may be slightly different from the background of the actual QBO due to the forcings of the two experiments.

The difference in the zonal wind and temperature forcings between the two experiments showed maxima at 30 hPa and 50 hPa, respectively (Figure 6). The difference between the zonal wind and temperature of the EQBO and WQBO in the observational data, which is shown in Son et

al. (2017), found maximum values at 50 hPa and 70 hPa, respectively. This means that the maximum value of zonal wind and temperature in this experiment is shown at higher altitudes than that of other QBO cases. In a recent model study, a lower QBO forcing can lead to a modulated MJO that is more active than a higher QBO forcing. Martin et al. (2019) conducted a single convection model with varying altitude and intensity differences in the vertical structure of zonal wind and temperature according to QBO. The results emphasize that a lower and stronger QBO forcing in the model can make the QBO-MJO connection better than a higher and weaker QBO forcing. The WQBO forcing in the WQBO simulation shows a weaker WQBO zonal wind profile than in the observations. If we select the case in which the maximum difference in zonal wind and temperature appears at lower altitudes and the difference becomes larger, we can expect a stronger MJO intensity difference between the two experiments.

The thermal structure in the upper troposphere is also quite different from that in Son et al. (2017). The vertical temperature structure in the previous study shows the warm (cold) temperature near 200-300 hPa in the EQBO (WQBO) winter. The warm temperature near 200-300 hPa and the cold temperature in the lower stratosphere can result in lower static stability. However, the temperature forcing in

the EQBO experiments is colder than that in the WQBO experiments in this study. This vertical temperature structure difference is thought to have contributed to the smaller MJO intensity difference between the two experiments than the observational data.

Despite these limitations, a difference in MJO intensity and structure according to the QBO between the two experiments, like in the observations, is also simulated in the model. Therefore, despite the difficulty in calculating statistical significance according to the small number of samples, it is thought that the results of this study can provide some indication of the relationship between the two phenomena. However, in this study, only the vertical structure difference between the two simulations is suggested. More detailed studies are needed to examine the exact physical and dynamical mechanisms in the QBO-MJO connection.

5. References

Ahn, M.-S., D. Kim, K. R. Sperber, I.-S. Kang, E. Maloney, D. Waliser, H. H. Hendon, and on behalf of WGNE MJO Task Force (2017), MJO simulation in CMIP5 climate models: MJO skill metrics and process-oriented diagnosis, *Clim. Dyn.*, **49**, 4023-4045.

Board, O. S., and National Academies of Sciences, and Medicine (2016), Next generation earth system prediction: Strategies for subseasonal to seasonal forecasts, Washington, DC: National Academies Press.

Butchart, N., J. A. Anstey, K. Hamilton, S. Osprey, C. McLandress, A. C. Bushell, Y. Kawatani, Y.-H. Kim, F. Lott, J. Scinocca, T. N. Stockdale, M. Andrews, O. Bellprat, P. Braesicke, C. Cagnazzo, C.-C Chen, H.-Y. Chun, M. Dobrynin, R.R. Garcia, J. Garcia-Serrano, L. J. Gray, L. Holt, T. Kerzenmacher, H. Naoe, H. Pohlmann, J. H. Richter, A. A. Scaife, V. Schenzinger, F. Serva, S. Versick, S. Watanabe, K. Yoshida, and S. Yukimoto (2018). Overview of experiment design and comparison of models participating in phase 1 of the SPARC Quasi-Biennial Oscillation initiative (QBOi), *Geosci. Model Dev.*, **11**, 1009–1032.

Chen, F., and J. Dudhia (2001), Coupling an advanced land surface-hydrology model with the Penn State–NCAR MM5 modeling system. Part I: Model implementation and sensitivity, *Mon. Wea. Rev.*, **129**, 569–585.

Chen, X., and F. Zhang (2019). Relative Roles of Preconditioning Moistening and Global Circumnavigating Mode on the MJO Convective Initiation During DYNAMO. *Geophys. Res. Lett.*, **46**, 1079-1087.

Chou, M. D., and M. J. Suarez (1994), An efficient thermal infrared radiation parameterization for use in general circulation models, NASA Tech. Memo. 104606, 98 pp.

Collimore, C. C., D. W. Martin, M. H. Hitchman, A. Huesmann, and D. E. Waliser (2003), On the relationship between the QBO and tropical deep convection, *J. Climate*, **16** (15), 2552–2568.

Dee, D. P., and Coauthors (2011), The ERA-Interim reanalysis: configuration and performance of the data assimilation system, *Q. J. R. Meteorel. Soc.*, **137,** 553-597.

Hendon, H. H., and S. Abhik (2018), Differences in vertical structure of the Madden-Julian Oscillation associated with the quasi-biennial oscillation, *Geophys. Res. Lett.*, **45**, 4419-4428.

Hong, S.-Y., Y. Noh, and J. Dudhia (2006), A new vertical diffusion package with an explicit treatment of entrainment processes, *Mon. Wea. Rev.*, **134**, 2318–2341.

Hung, M.-P., J.-L. Lin, W. Wang, D. Kim, T. Shinoda, and S. J. Weaver (2013), MJO and convectively coupled equatorial waves simulated by CMIP5 climate models, *J. Climate*, **26**, 6185–6214.

Iacono, M. J., J. S. Delamere, E. J. Mlawer, M. W. Shephard, S. A. Clough, and W. D. Collins (2008), Radiative forcing by long-lived greenhouse gases: Calculations with the AER radiative transfer models, *J. Geophys. Res.*, **113**. D13103.

Kim, D., H. Kim, and M.-I. Lee (2017), Why does the MJO detour the Maritime Continent during austral summer? *Geophys. Res. Lett.*, **44**, 2579-2587.

Klemp, J. B., J. Dudhia, and A. D. Hassiotis (2008), An upper gravity-wave absorbing layer for NWP applications, *Mon. Wea. Rev.*, **136**, 3987–4004.

Loeb, N. G., S. Kato, W. Su, T. Wong, F. G. Rose, D. R. Doelling, J. R. Norris, and X. Huang (2012), Advances in understanding top-of-atmosphere radiation variability from satellite observations. Surv. Geophys., **33**, 359–385.

Lee J.C.K., and N.P. Klingaman (2018). The effect of the quasi-biennial oscillation on the Madden–Julian oscillation in the Met Office Unified Model Global Ocean Mixed Layer configuration. *Atmos. Sci. Lett.*. **19**, e816.

Lim, K.-S. S., and S.-Y. Hong (2010), Development of an effective double-moment cloud microphysics scheme with prognostic cloud condensation nuclei (CCN) for weather and climate models, *Mon. Wea. Rev.*, **138**, 1587–1612.

Lim, Y., S.-W. Son, A. G. Marshall, H. H. Hendon, and K.-H., Seo (2019). Influence of the QBO on MJO prediction skill in the sub seasonal-to-seasonal prediction models. *Clim. Dyn.*, **53**, 1681-1695.

Lin, J.-L., and Coauthors (2006), Tropical intraseasonal variability in 14 IPCC AR4 climate models. Part I: Convective signals, *J.*

Climate, **19**, 2665–2690.

Madden, R. A., and P. R. Julian (1971), Detection of a 40–50 day oscillation in the zonal wind in the tropical Pacific, *J. Atmos. Sci.*, **28**, 702–708.

Madden, R. A., and P. R. Julian (1972), Description of global-scale circulation cells in tropics with a 40–50 day period, *J. Atmos. Sci.*, **29**, 1109–1123.

Marshall, A. G., H. H. Hendon S.-W. Son, and Y. Lim (2017), Impact of the quasi-biennial oscillation on predictability of the Madden–Julian oscillation, *Clim. Dyn.*, **49**(4), 1365–1377.

Martin, Z., S. Wang, J. Nie, and A. Sobel (2019), The Impact of the QBO on MJO Convection in Cloud-Resolving Simulations, *J. Atmos. Sci.*, **76**, 669-688.

Nishimoto, E., and S. Yoden (2017). Influence of the stratospheric quasi-biennial oscillation on the Madden–Julian Oscillation during austral summer. J. Atmos. Sci., 74(4), 1105–1125. https://doi.org/10.1175/JAS-D-16-0205.1

Shi, J. J., and Coauthors (2010), WRF simulations of the 20–22 January 2007 snow events over eastern Canada: Comparison with in situ and satellite observations, *J. Appl. Meteor. Climatol.*, **49**, 2246–2266.

Skamarock, W. C., and Coauthors (2008), A description of the Advanced Research WRF version 3. NCAR Tech. Note NCAR/TN- 4751STR, 125 pp.

Son, S.-W., Y. Lim, C. Yoo, H. H. Hendon, and J. Kim (2017), Stratospheric control of Madden–Julian oscillation, *J. Climate*, **30**, 1909–1922.

Waliser, D. E., and Coauthors (2006), The Experimental MJO Prediction Project, *Bull. Amer. Meteor. Soc.*, **87,** 425–431.

Wang, S., A. H. Sobel, F. Zhang, Y. Sun, Y. Yue, and L. Zhou (2015), Regional simulation of the October and November MJO events observed during the CINDY/DYNAMO field campaign at gray zone resolution, *J. Climate*, **28**, 2097–2119.

Wielicki, B. A., B. R. Barkstrom, E. F. Harrison, E. B. Lee III, G. L. Smith, and J. E. Cooper (1996), Clouds and the Earth's Radiant Energy System (CERES): An Earth Observing System experiment. Bull. Amer. Meteor. Soc., 77, 853–868.

Yoo, C., and S.-W. Son (2016), Modulation of the boreal wintertime

Madden-Julian oscillation by the stratospheric quasi-biennial oscillation, *Geophys. Res. Lett.*, **43**, 1392-1398.

Zeng, X., and A. Beljaars (2005), A prognostic scheme of sea surface skin temperature for modeling and data assimilation, *Geophys. Res. Lett.*, **32**, L14605.

Zhang, C. (2005), Madden-Julian oscillation, *Rev. Geophys*., **43**, RG2003.

Zhang, C., J. Gottschalck, E. D. Maloney, M. W. Moncrieff, F. Vitart, D. E. Waliser, B. Wang, and M. C. Wheeler (2013), Cracking the MJO nut, *Geophys. Res. Lett.*, **40**, 1223–1230.

Zhang, C., and B. Zhang (2018), QBO-MJO connection, *J. Geophys. Res. Atmos.*, **123**, 2957–2967.

Zhang, F., S. Taraphdar, and S. Wang (2017), The role of global circumnavigating mode in the MJO initiation and propagation, *J. Geophys. Res. Atmos.*, **122** (11), 5837-5856.

6. Tables

Table 1. The Weather Research and Forecasting (WRF) model configuration for the 2007 December MJO event. The physics scheme, dynamics scheme, and boundary conditions are identical to those of Wang et al. (2015).

Model	Weather Research and Forecasting model (WRF) V.3.4.1	
Horizontal grid	9 km × 9 km	
Model top	20 hPa (L45)	
Study region	Longitude : 50 – 150ºE, Latitude : 20ºS – 20ºN	
Boundary Condition	Lateral Boundary : narrow transition zone of 5 grid points, tendencies are prescribed every 6 hour	
	Oceanic portion of lower boundary : SST updated every 6 hour	
	Using ERA-Interim to prescribe	
	Applying spectral nudging (zonal wavenumber : 0-4, meridional wavenumber : 0-2) to relax horizontal wind fields for first three days.	
Physics Scheme	Land Surface	Unified Noah land physics scheme (Chen and Dudhia, 2001)
	Skin Temperature	Surface skin temperature scheme (Zeng and Belijaars, 2005)
	PBL scheme	YSU PBL scheme (Hong et al., 2006)
	Microphysics	WDM microphysics scheme from WRF V3.5.1 (Lim and Hong, 2010)
	Longwave Radiation	RRTMG (Iacono et al., 2008)
	Shortwave Radiation	Updated Goddard shortwave scheme (Chou and Suarez, 1994; Shi et al., 2010)
	Surface fluxes	Monin-Obukov scheme
Dynamics Scheme	horizontal advection	5th order accurate
	Vertical advection	3rd order accurate
	Moisture and condensate advection	Positive definite scheme
	Suppress vertically propagating gravity waves	Implicit damping scheme (Klemp et al., 2008)
	Horizontal turbulent eddy mixing	Smagorinsky 1st order closure

Table 2. Ensemble members and their initialization times, which are used in this study.

Ensemble Number	Initialization time
Ensemble 1	00UTC 20NOV2007
Ensemble 2	12UTC 20NOV2007
Ensemble 3	00UTC 21NOV2007
Ensemble 4	12UTC 21NOV2007
Ensemble 5	00UTC 22NOV2007
Ensemble 6	12UTC 22NOV2007
Ensemble 7	00UTC 23NOV2007
Ensemble 8	12UTC 23NOV2007

7. Figures

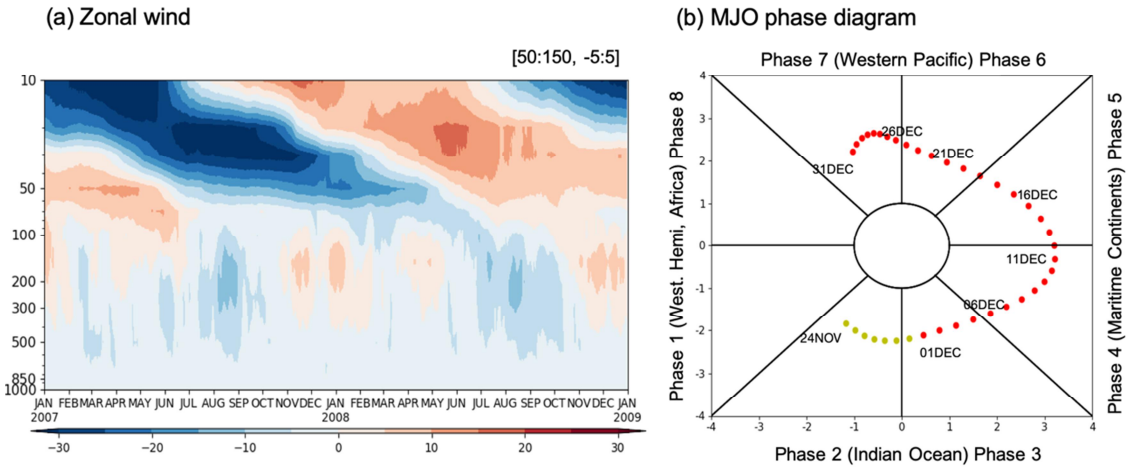

Figure 1. (a) Time-height diagram of zonal wind (shading: m s^{-1}) averaged over 50–150°E, 5°S–5°N from January 2007 to December 2008 and (b) MJO phase diagram with OMI index from November 24 to December 31, 2007.

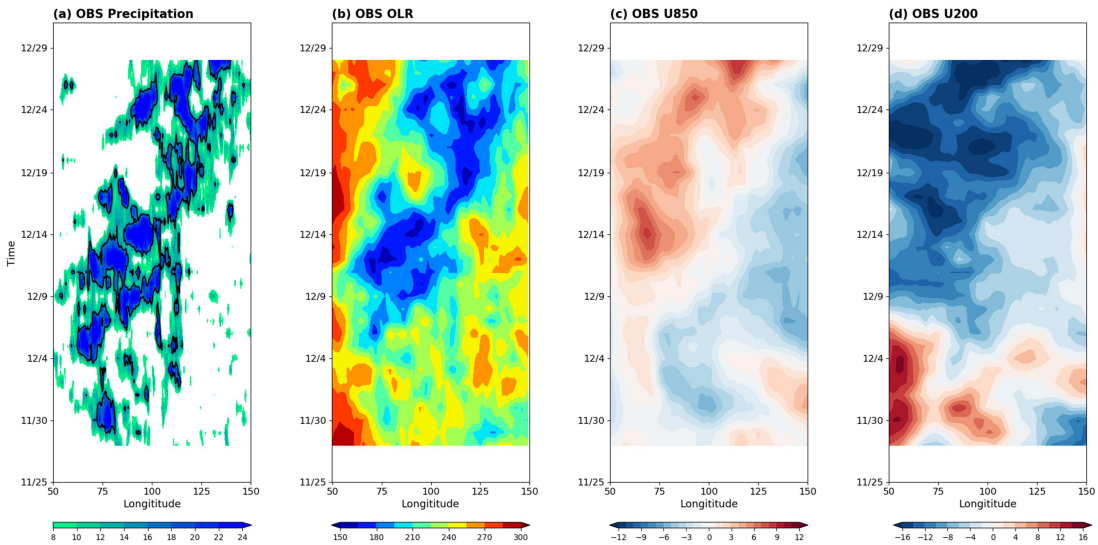

Figure 2. Time-longitude diagrams of (a) precipitation (shading: mm day^{-1}, contour: 15 mm day^{-1}), (b) outgoing longwave radiation (OLR) (shading: W m^{-2}), (c) 850-hPa and (d) 200-hPa zonal wind (shading: m s^{-1}) averaged over latitudes of 15°S–5°N based on observational datasets.

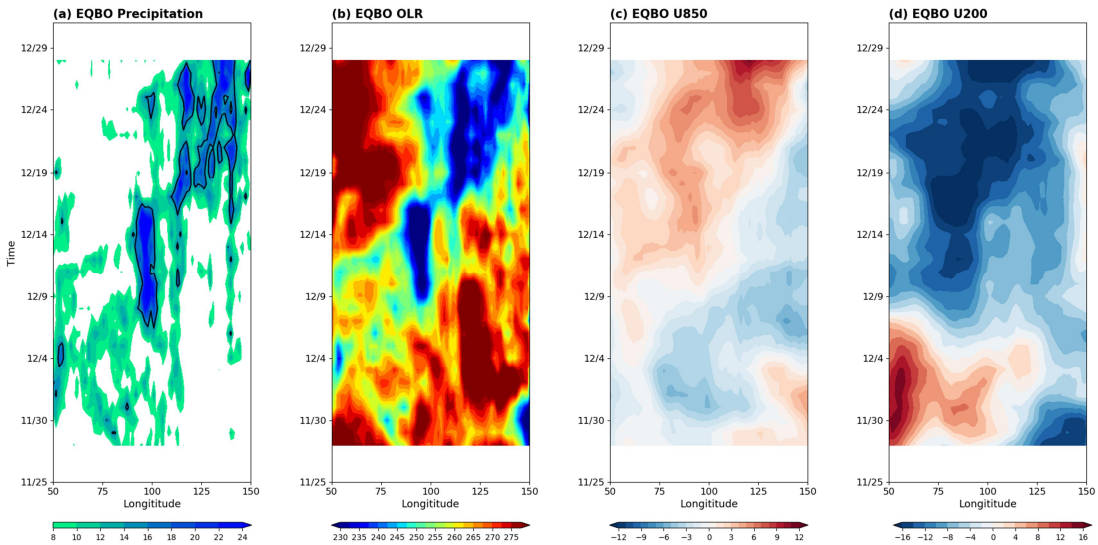

Figure 3. Time-longitude diagrams of (a) precipitation (shading: mm day^{-1}, contour: 15 mm day^{-1}), (b) OLR (shading: W m^{-2}), (c) 850-hPa and (d) 200-hPa zonal wind (shading: m s^{-1}) averaged over latitudes of 15°S–5°N based on the EQBO experiments.

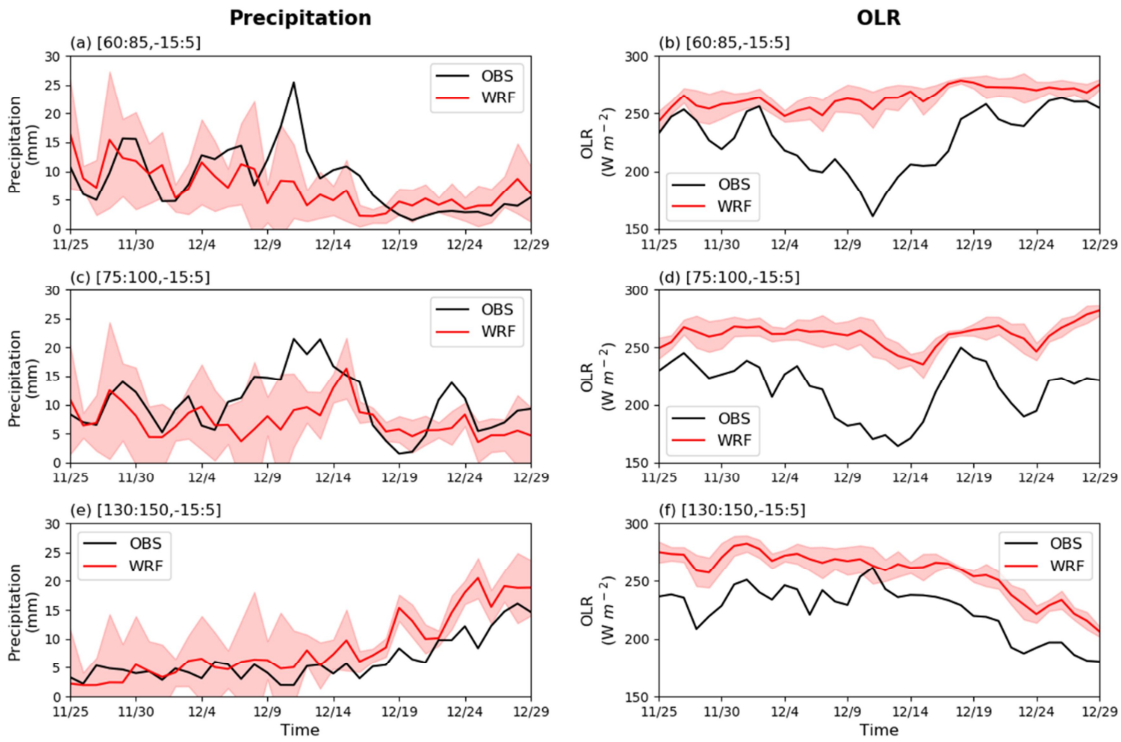

Figure 4. The time-series of precipitation (left column: mm day^{-1}) and OLR (right column: W m^{-2}) in the Indian Ocean (upper panel), west of the Maritime Continents (middle panel), and the Maritime Continents (lower panel).

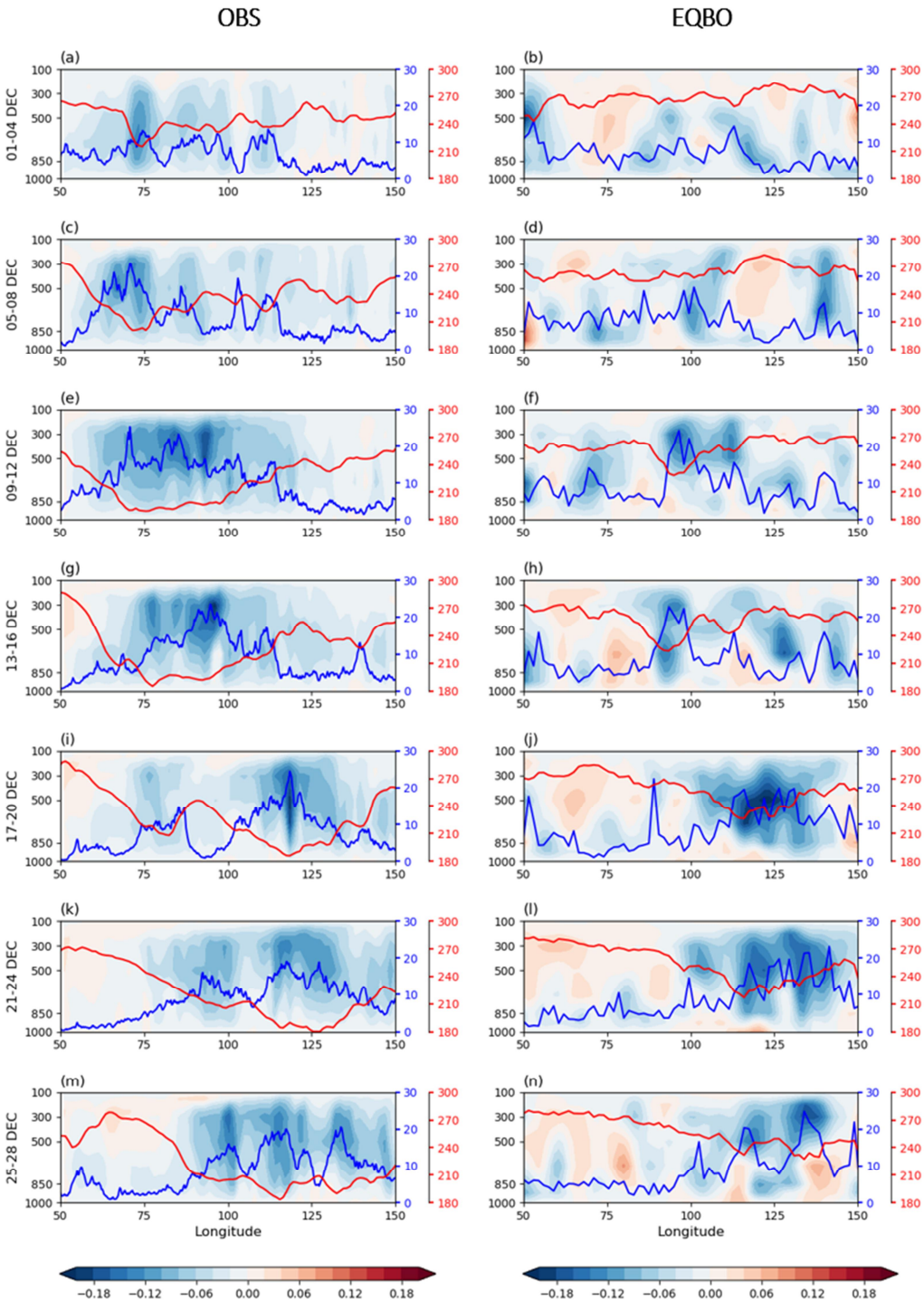
OBS
EQBO
(a)
(b)
(c)
(d)
(e)
(f)
(g)
(h)
(i)
(j)
(k)
(l)
(m)
(n)
01-04 DEC
05-08 DEC
09-12 DEC
13-16 DEC
17-20 DEC
21-24 DEC
25-28 DEC
Longitude
Longitude
−0.18 −0.12 −0.06 0.00 0.06 0.12 0.18
−0.18 −0.12 −0.06 0.00 0.06 0.12 0.18

Figure 5. The longitude-height diagrams of pressure velocity (shading: Pa s^{-1}) and zonal distribution of precipitation (blue line: mm day^{-1}) and OLR (red line: W m^{-2}) averaged over latitudes of 15°S–5°N. Each composite map is averaged for four days from December 1 to 31, 2007. The left and right columns show the observations and EQBO experiments, respectively.

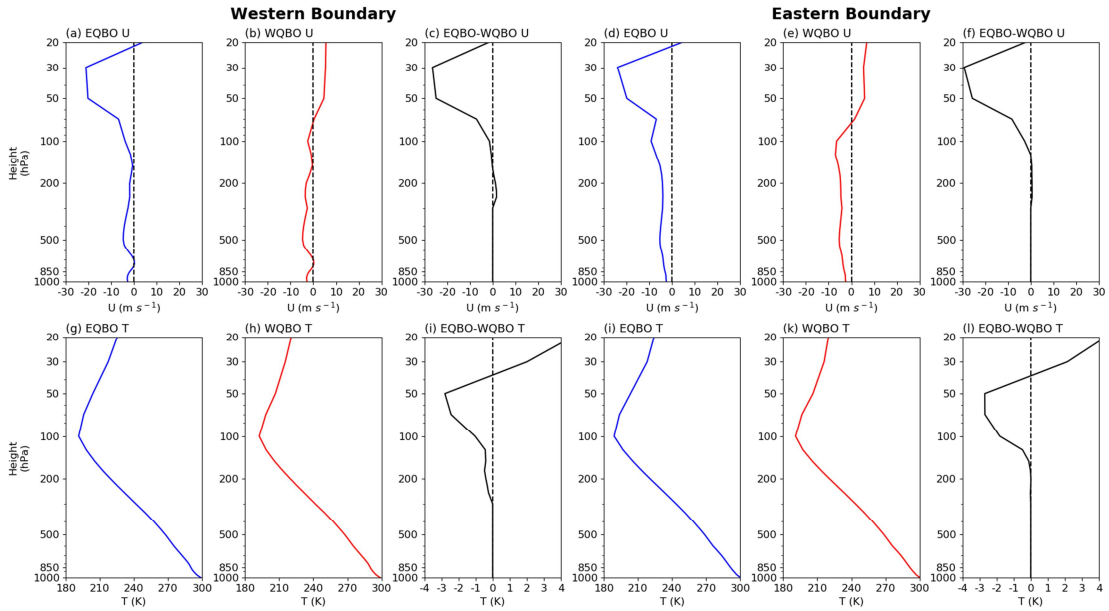

Figure 6. The vertical profile of zonal wind (unit: m s^{-1}) and temperature (unit: K) averaged over latitudes of 5°S–5°N in the western (50°E) and eastern (150°E) boundary of the model from November 24 to December 31, 2007.

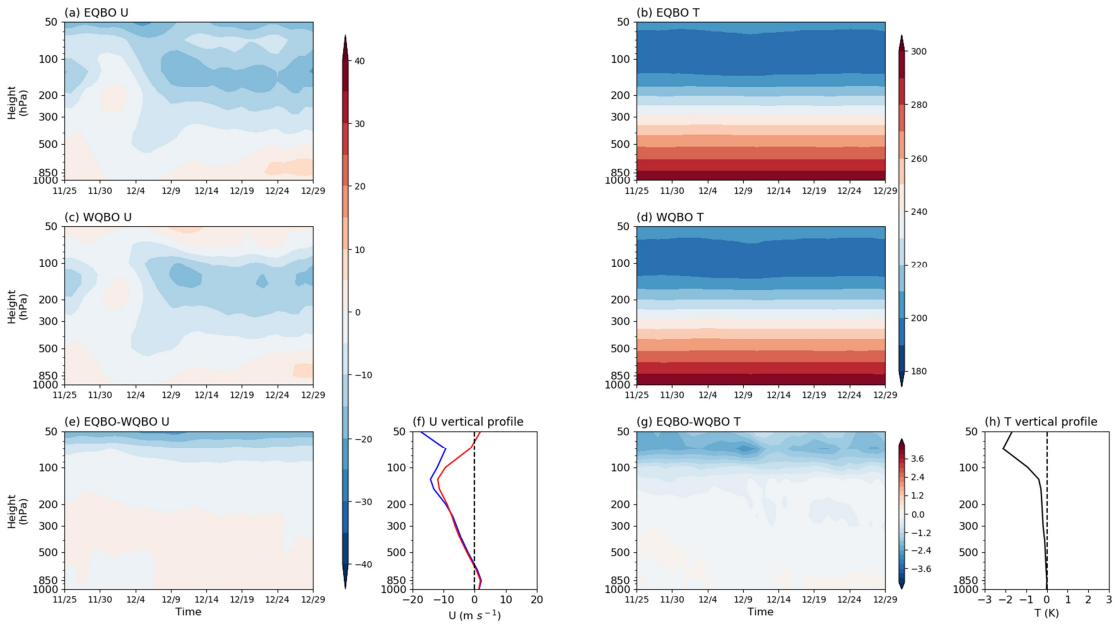

Figure 7. The time-height diagrams of zonal wind (leftmost column: m s^{-1}) and temperature (second rightmost column: K) averaged over latitudes of 5°S-5°N in the EQBO (upper panel) and WQBO (middle panel) experiments and the difference between the two experiments from November 25 to December 29, 2007. The vertical profile of (f) zonal wind in the EQBO and WQBO experiments and (h) the temperature difference between the EQBO and WQBO experiments averaged from November 24 to December 31, 2007.

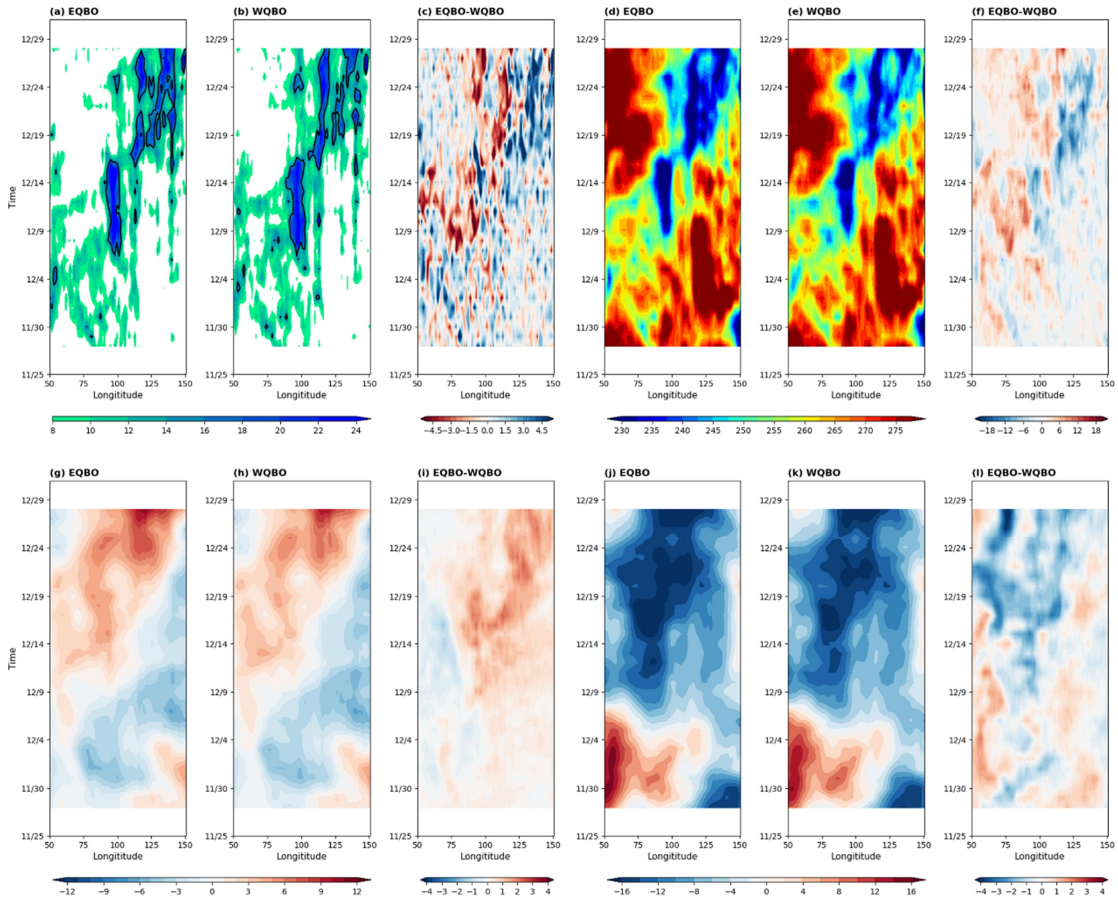

Figure 8. Time-longitude diagrams of (a)-(c) precipitation (shading: mm day^{-1}, contour: 15 mm day^{-1}), (d)-(f) OLR (shading: W m^{-2}), (g)-(i) 850-hPa and (j)-(l) 200-hPa zonal wind (shading: m s^{-1}) averaged over latitudes of 15°S–5°N from the EQBO and WQBO experiments and the difference between the two experiments.

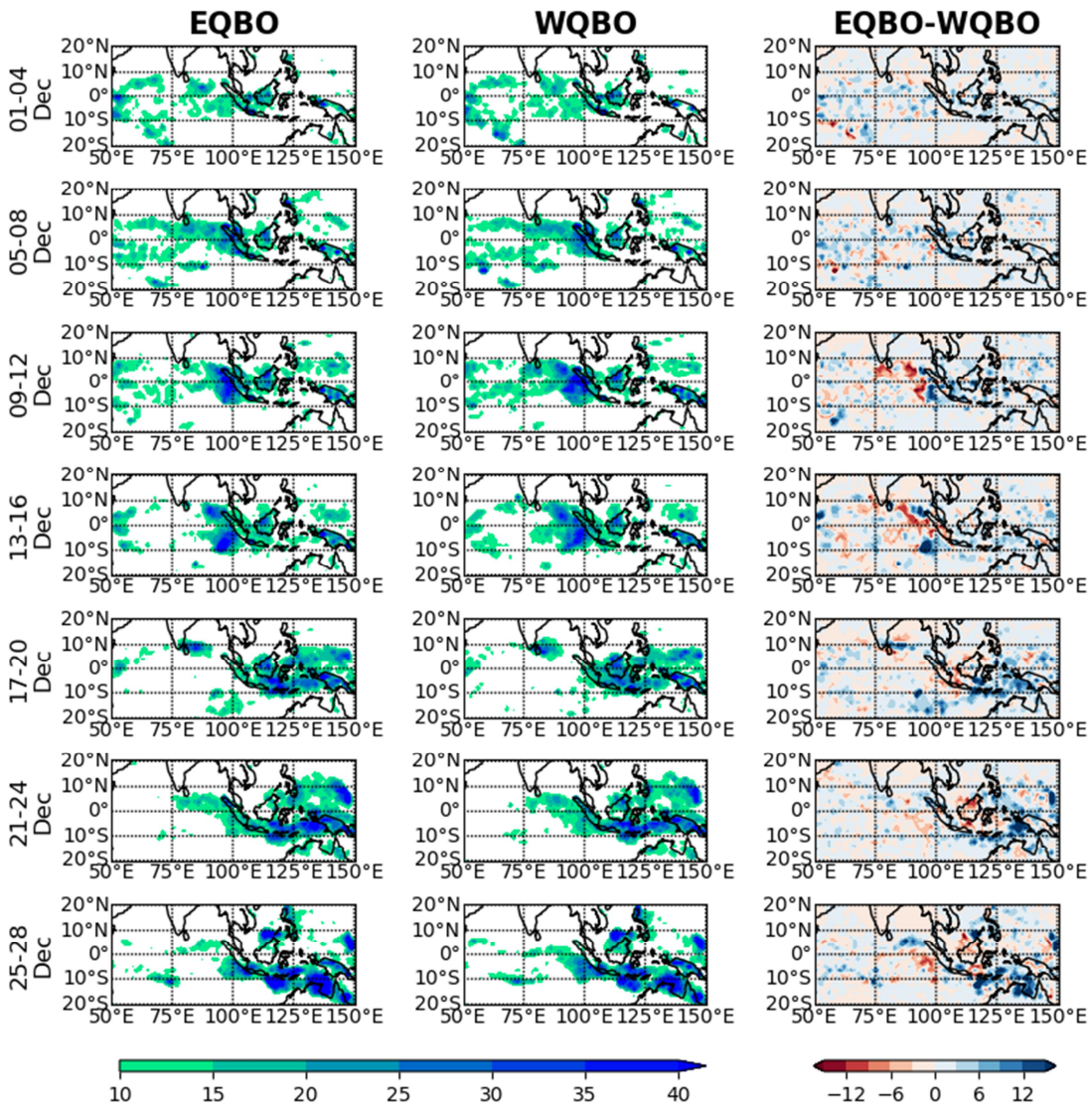

Figure 9. The longitude-latitude diagrams of precipitation (shading: mm day^{-1}). Each composite map is averaged from for four days beginning on December 1, 2007. The left, middle and right columns show the EQBO, WQBO, and the difference between the two experiments, respectively.

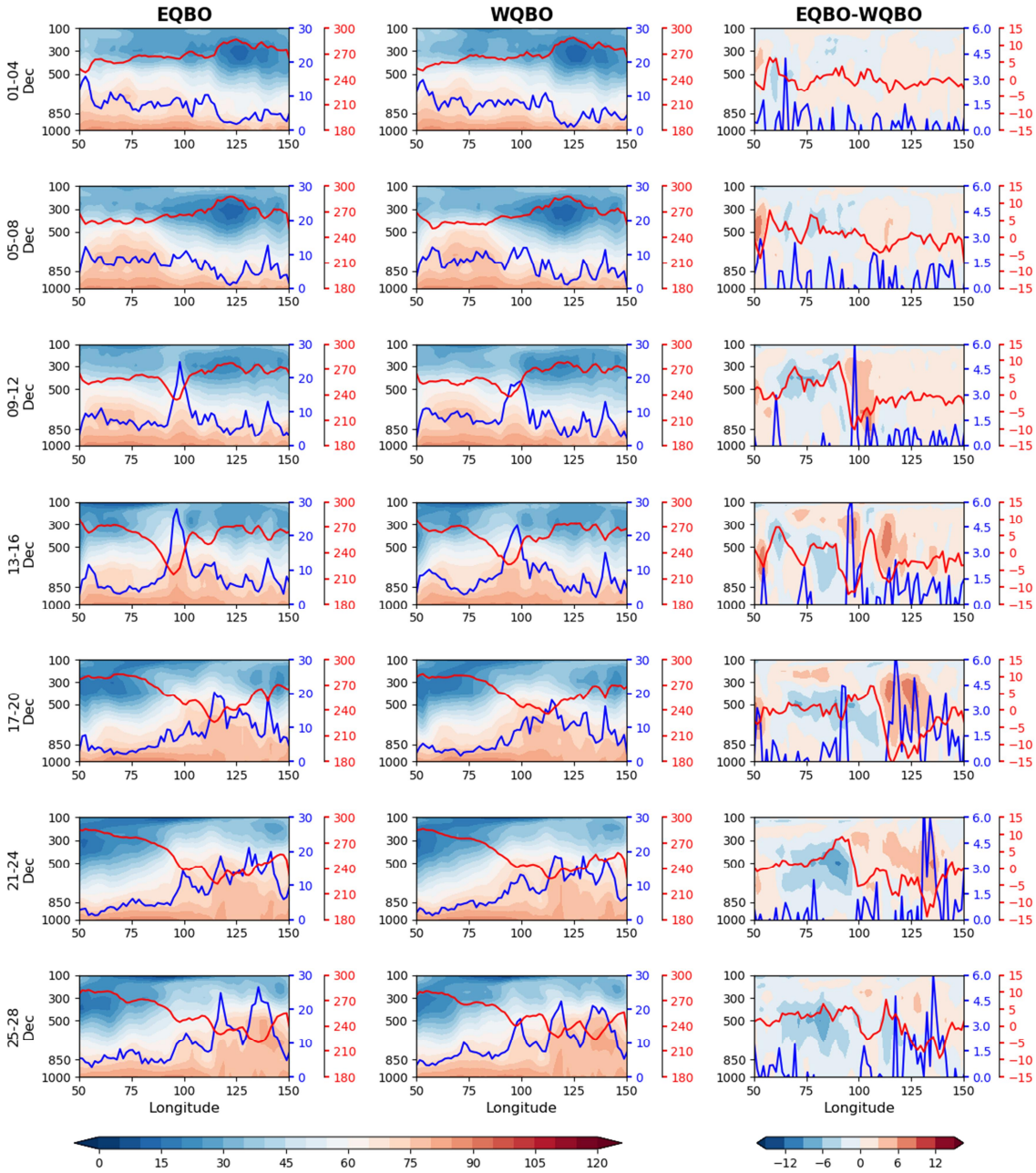

Figure 10. The longitude-height diagrams for the 15°S–0° averaged relative humidity (shading: %) and zonal distribution of precipitation (blue line: mm day^{-1}) and OLR (red line: W m^{-2}). Each composite map is averaged for four days beginning on December 1, 2007. The left middle and right

columns show the EQBO, WQBO, and the difference between the two experiments, respectively.

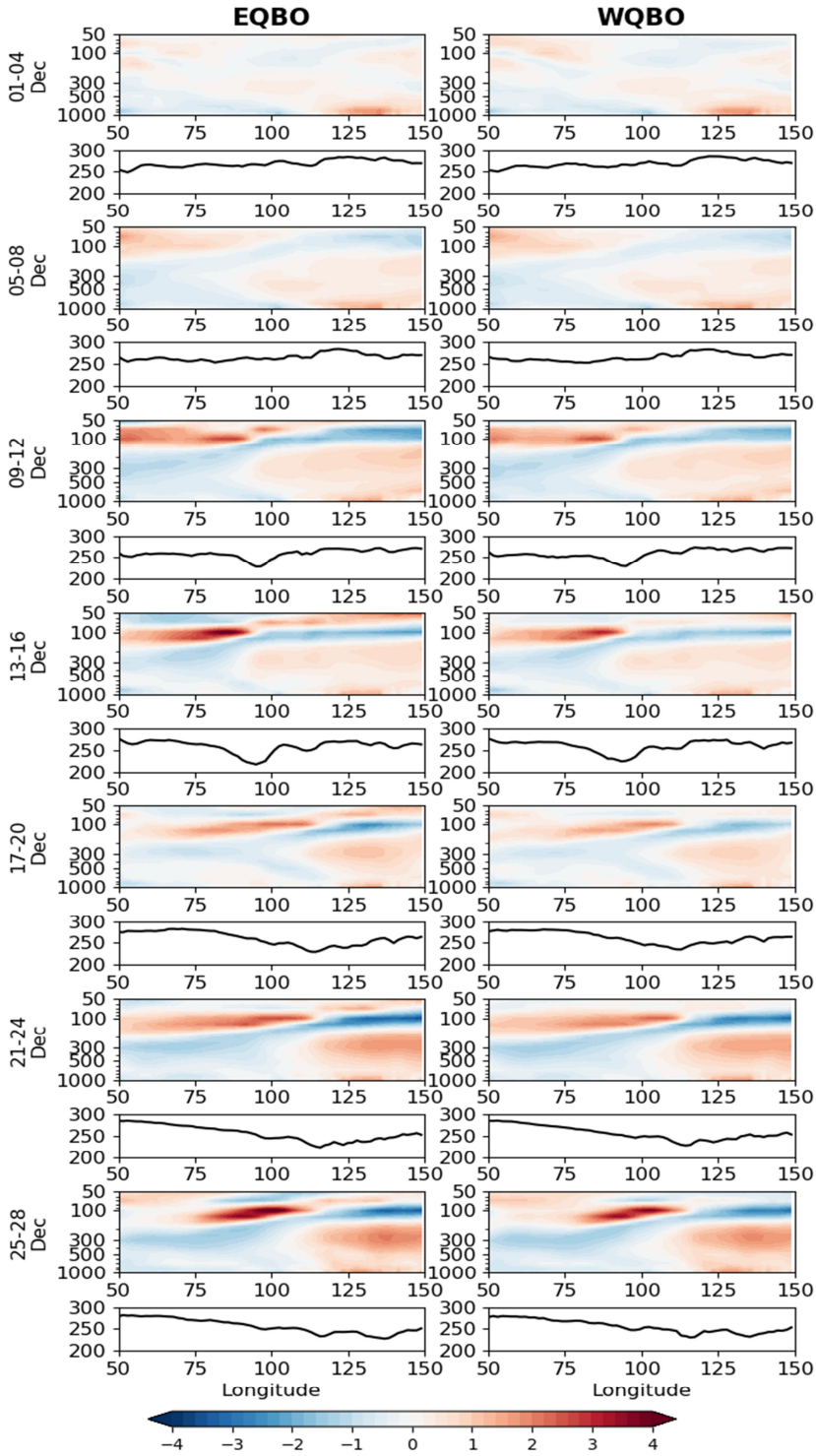
EQBO
WQBO
01-04 Dec
05-08 Dec
09-12 Dec
13-16 Dec
17-20 Dec
21-24 Dec
25-28 Dec
50
100
300
500
1000
300
250
200
50
75
100
125
150
Longitude
−4
−3
−2
−1
0
1
2
3
4

Figure 11. The longitude-height diagrams for the 15°S–5°N averaged temperature deviation from the domain zonal mean (shading: K) and zonal distribution of OLR (black line: W m^{-2}). Each composite map is averaged for four days beginning on 1 December 2007. The left panel and figure show the composite map in the EQBO and WQBO experiments, respectively.

초 록

수치 모델에서 나타난 QBO 의 MJO 조절효과

백승윤
지구환경과학부
석사과정
서울대학교

매든-줄리안 진동(Madden-Julian Oscillation; MJO)과 준 2 년 주기 진동(Quasi-Biennial Oscillation; QBO) 사이의 관계는 최근 많은 연구들에서 밝혀졌다. 성층권의 동서방향 바람이 동풍(Easterly QBO; EQBO)일 때, 서풍(Westerly QBO; WQBO)일 때보다 MJO 의 활동성은 더 강해지는 것으로 나타났다. 이러한 관계가 재분석자료에서 잘 나타남에도 불구하고, 수치모델에서는 두 관계의 모의에 어려움을 겪어왔다. 본 연구에서는 WRF 모델을 이용하여 QBO 의 배경장이 MJO 에 영향을 미칠 수 있는지 검증해보고자 한다. 분석을 위해 2007 년 12 월의 EQBO 의 경계조건을 가지는 MJO 사례를 모의하는 실험(EQBO 실험)을 구성하였고, 경계조건으로 들어가는 재분석자료에서 1.5-3 년의 주기의 성분을 Lanczos 필터링하여

제거해줌으로서 WQBO 의 경계조건을 가지는 실험(WQBO 실험)을 구성하였다. 그 결과, EQBO 실험에서 WQBO 실험보다 더 강한 강수 반응이 Maritime Continents 부근에서 나타났다. 또한 EQBO 실험에서 MJO 강수강화로 인한 MJO 대류의 상부에 형성되는 음의 기온 아노말리 지역이 관측과 유사하게 WQBO 실험에 비해 더 넓고 차가운 지역이 형성되는 것이 확인되었다. 이러한 결과는 수치모델을 통해 QBO 와 MJO 간의 관계가 모의 가능함을 보여주었고, 이를 통해서 QBO 와 MJO 간의 물리적, 역학적 관계를 이해할 수 있는 가능성을 시사한다.

주요어: 매든-줄리안 진동,준 2 년 주기진동, WRF 모델
학번: 2018-24809